minerals

MDPI

Article

Geochronology and Geochemistry of Cretaceous Adakitic Rocks of the Dongguashan Cu Deposit in the Lower Yangtze River Belt: Insights into Petrogenesis and Mineralization

Zanzan Zhang [1,2,3], Xiaoyan Jiang [1,*], Jia Guo [4] and Kenan Jiang [1]

[1] State Key Laboratory of Ore Deposit Geochemistry, Institute of Geochemistry, Chinese Academy of Sciences, Guiyang 550081, China
[2] School of Earth and Space Sciences, University of Science and Technology of China, Hefei 230026, China
[3] Geological Survey of Anhui Province (Anhui Institute of Geological Sciences), Hefei 230001, China
[4] College of Earth Sciences, Chengdu University of Technology, Chengdu 610059, China
* Correspondence: jiangxiaoyan@mail.gyig.ac.cn

Abstract: The Lower Yangtze River Belt (LYRB) is a well-known and important base area with regard to Cu polymetallic resources in China. Large Cu polymetallic deposits in the LYRB are strongly associated with Cretaceous adakitic rocks. However, the petrogenesis of the Early Cretaceous adakites and the temporal–genetic relationship with mineralization are still disputable. The Dongguashan (DGS) Cu polymetallic deposit in the Tongling ore cluster is one of the largest Cu deposits in the LYRB. The DGS intrusion mainly comprises quartz monzodiorite, with SiO_2 contents varying from 63.7 to 67.9 wt%. Zircons from the quartz monzonite yield a SIMS U-Pb age of 138.9 ± 1.8 Ma, which indicates that the Cretaceous magmatism is coeval with mineralization. The studied rocks show typical geochemical signatures of adakites, characterized by high Al_2O_3 (14.9–16.2 wt%) and Sr (800–910 ppm) and low Y (15.2–17.5 ppm) and Yb (1.37–1.52 ppm) contents, with consequently high Sr/Y (46–61) and $(La/Yb)_N$ (14.8–18.5) ratios. The zircon $\delta^{18}O$ values of the DGS adakites range from 5.7‰ to 7.3‰, indicating a heterogeneous source. Whole-rock Sr-Nd isotopic compositions show an enriched character, with I_{Sr} ratios from 0.70783 to 0.70794 and $\varepsilon_{Nd}(t)$ values around −11.0, which fall intermediately in the area of MORB (mid-ocean ridge basalt), marine sediment, and the ancient lower crust. Comprehensively, whole-rock geochemical compositions and isotopic values suggest that the adakites are generated from the partial melting of the subducted oceanic crust and possibly with the involvement of sedimentary materials derived from the slab or continental crust. Moreover, the bulk-rock high-Cu composition, and the physical–chemical conditions (high oxygen fugacity and high volatile contents) revealed by apatites, plays critical roles in the formation of Cu mineralization in the DGS Tongling ore cluster, LYRB.

Keywords: adakite; Cretaceous; Cu mineralization; Dongguashan; Tongling ore cluster; LYRB

Citation: Zhang, Z.; Jiang, X.; Guo, J.; Jiang, K. Geochronology and Geochemistry of Cretaceous Adakitic Rocks of the Dongguashan Cu Deposit in the Lower Yangtze River Belt: Insights into Petrogenesis and Mineralization. *Minerals* **2023**, *13*, 953. https://doi.org/10.3390/min13070953

Academic Editor: Jean-Michel Lafon

Received: 29 June 2023
Revised: 9 July 2023
Accepted: 14 July 2023
Published: 17 July 2023

1. Introduction

The LYRB is one of the most important Late Mesozoic magmatic belts and metallogenic provinces in Eastern China [1–3]. Over 200 Mesozoic magmatic polymetallic (Cu, Fe, Au, Mo, Zn, Pb, and Ag) ore deposits have been discovered along the LYRB. From west to east, these polymetallic deposits can be divided into seven ore clusters: Edong, Jiurui, Anqing-Guichi, Luzong, Tongling, Ningwu, and Ningzhen, respectively [2,4,5]. These polymetallic ore deposits are not only temporally associated with but also genetically related to adakitic rocks in this region [1,4–8]. Many studies on preliminary geology and geochemistry have been well-conducted and established the relationships between polymetallic mineralization, magmatism, stratigraphy, and tectonics [2,9–11]. Mainly three stages of magmatism and mineralization in the LYMB can be classified based on the field investigation along with collected geochronological data: (1) the first stage (148–135 Ma),

intermediate-acid intrusions linked to Cu-Au-Mo polymetallic mineralization; (2) the second stage (133–127 Ma), mafic-intermediate volcanic and subvolcanic rocks associated with magnetite–apatite deposits; and (3) the third stage (129–120 Ma), A-type granites and alkaline rocks with U-Au mineralization [5,7,12–18]. Previous studies suggest that the first episode of high-K calc-alkaline intermediate-acid intrusions is congruously recognized to have adakitic-like features [7,8,17,19]. However, the origins of the ore-bearing adakites in the ore clusters are still debated and can be summarized as follows: (1) partial melting of the subducted oceanic slab of the Paleo-Pacific plate or metasomatized mantle wedge [6–8,17,20,21]; (2) partial melting of the thickened or delaminated lower continental crust [22–25]; (3) generated from mantle-derived magma following assimilation and fractional crystallization [1,26–29]; and (4) mixing of the mantle-derived and crust-derived magmas [11,30–34].

Accessory minerals in magmatic rocks provide a window into the petrogenesis and ore-forming mechanism for preserving a wealth of information on source components, magmatic evolution, and related mineralization. Both zircon and apatite are robust, long-lasting, and ubiquitous minerals in magmatic rocks. Zircon can preserve the magmatic O isotopic compositions, which is a useful proxy for the primary oxygen isotopic composition in magmas [35]. The mantle is a remarkably homogeneous oxygen isotope reservoir, and igneous oxygen isotopes of zircons in equilibrium with pristine mantle-derived melts have a well-constrained and narrow range of $\delta^{18}O$ values (5.3 ± 0.3‰, 1SD) [36,37]. Moreover, zircon oxygen isotopic values ($\delta^{18}O_{Zrc}$) are insusceptible to fractional crystallization due to fractionation $\Delta^{18}O_{(WR\text{-}Zrc)}$ increasing at nearly the same rate as $\delta^{18}O_{(WR)}$ in the more evolved and silicic magmas. Apatite is also an important accessory mineral, which is the main host of the volatiles and has great importance in metallogenic studies, especially with regard to the magmatic processes and physio-chemical conditions [16,38–44].

The DGS deposit, discovered in 1974, is a representative Cu(-Au) ore deposit (0.94 Mt at 1.01% Cu and 22 t at 0.24 g/t Au) in the Tongling ore cluster [11]. The Mesozoic intermediate-acidic magmatic rocks widely developed in DGS are tightly associated with Cu polymetallic mineralization [11,45–47]. Knowledge about the petrology and genesis of the Cretaceous intermediate-acidic intrusions is important for revealing the petrogenesis and metallogenesis of the DGS deposit. Therefore, it is of great significance for understanding the petrological nature of the DGS quartz monzodiorite, which provides better constraints on the deposit genesis. This paper focuses on zircon U-Pb dating, O isotopic composition, and bulk rock elemental and Sr-Nd isotopic data of the DGS adakites, which are employed to provide insights into the petrogenesis and metallogenic mechanisms of the ore-bearing intrusion of the DGS deposit, the Tongling ore cluster, in the LYRB.

2. Geological Background

The LYRB is located along the northern margin of the Yangtze Craton and south of the Qinling–Dabie orogenic belt (Figure 1a). The 'V-shaped' metallogenic belt is bounded by the northwestern trending Xiangfan–Guangji and Tan–Lu faults and the southeastern trending Chongyang–Changzhou fault (Figure 1b; [4,48]). Extensive Late Mesozoic magmatism and large-scale mineralization occurred in the belt (Figure 1b,c; [2,4]). The Tongling ore cluster located in the central part of the LYRB, is one of the seven major mining regions in the metallogenic belt (Figure 1b). A total of 45 deposits and 76 plutons have been discovered within the district [2]. It comprises three major tectono-stratigraphic units: (1) an Archean to Late Proterozoic metamorphic basement, consisting of a Late Archean to Early Proterozoic metamorphic core complex and a thick flysch sequence intercalated with submarine volcanic rocks and intruded by Late Proterozoic granitioids; (2) a Paleozoic to Early Mesozoic marine sedimentary layer, including Carboniferous carbonate rocks, Permian black shale and limestone, and Triassic argillaceous rocks and carbonate rocks, except for the Middle–Late Devonian Cambrian to Early Triassic marine sediment coverage, including shale, siltstone, and limestone; and (3) Early Mesozoic to Late Mesozoic (Middle Triassic to Cretaceous) volcanic sequences and thick terrestrial sediments are widely covered

above those marine deposits, comprising Jurassic and Cretaceous extensive volcanic and intrusive rocks [1,2]. These widespread plutons are developed along the EW-trending Tongling–Nanling fault and intrude Silurian–Triassic sedimentary host rocks. The shape of the Late Mesozoic magmatic rocks is constrained by a series of NE-trending faults and folds. Numerous polymetallic Cu–Au deposits are products of those intermediate–felsic magmatic and relevant hydrothermal activities (Figure 1b) [49]. Ore-bearing intrusions include the DGS, Tongguanshan, Fenghuangshan, Xinqiao, and Shizishan, which mainly consist of intermediate-felsic magmatic rocks, including pyroxene monzodiorite, quartz monzodiorite, and granodiorite [15,50].

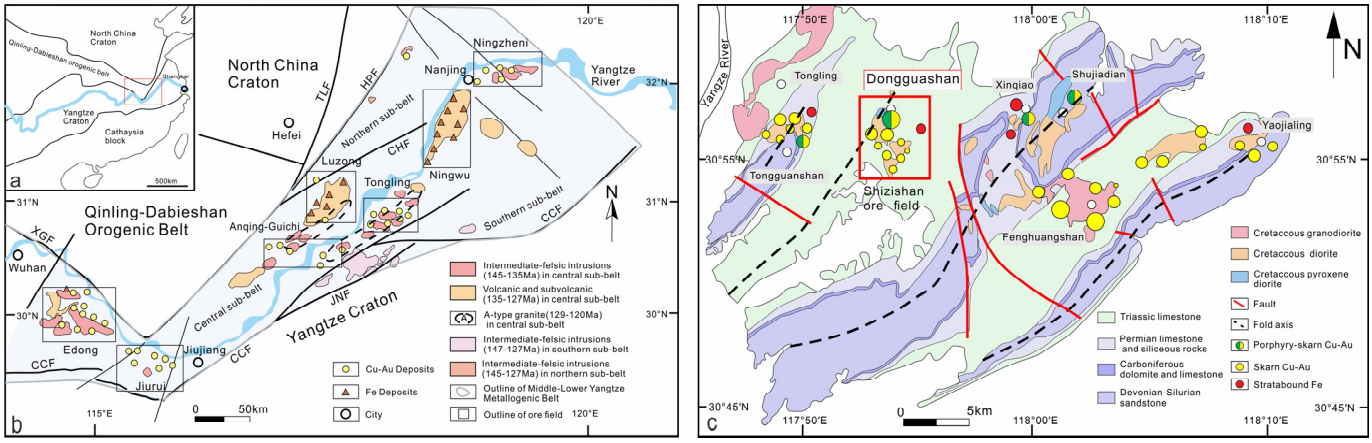

Figure 1. (**a**) Sketch map with the location of the LYRB; (**b**) Simplified geological map of intrusive and volcanic rocks and ore clusters in the LYRB (modified after Zhou et al. [48]; Mao et al. [4]); (**c**) Geological map of Tongling ore cluster, Anhui province (modified after Chang et al. [1]). TLF: Tancheng–Lujiang fault; XGF: Xiangfan–Guangji fault; HPF: Huanglishu–Poliangting fault; CHF: Chuhe fault; CCF: Chongyang–Changzhou fault; JNF: Jiangnan fault.

DGS is one of the economically most important polymetallic Cu-Au deposits in the Shizishan ore field, the Tongling ore cluster (Figure 1c) [1], and is located at the intersection of the NE-trending Qingshan anticline and the E-trending Tongling–Shatanjiao fold belt [51]. The sedimentary rocks exposed in the area are recognized to be Middle–Upper Silurian to Lower Triassic, with the exception of Lower to Middle Devonian rocks. Major structures consist of the NE-trending Qingshan anticline and the E-trending Datuanshan–Baoerling fault and control the emplacement of regional plutons and orebodies [51]. Quartz monzodiorite, closely related to Cu-Au mineralization [32], is intruded into Silurian to Triassic sedimentary strata [9]. Twelve fresh samples were collected from the drilling core (Figure S1). The samples were mainly quartz monzodiorite, which was light gray in color and medium- to coarse-grained in texture and had a massive structure. They consisted of plagioclase (45–60 vol%), potassium feldspar (10–20 vol%), quartz (5–15 vol%), and small amounts of biotite (Figure 2). Accessory minerals included zircon, apatite, titanite, and magnetite.

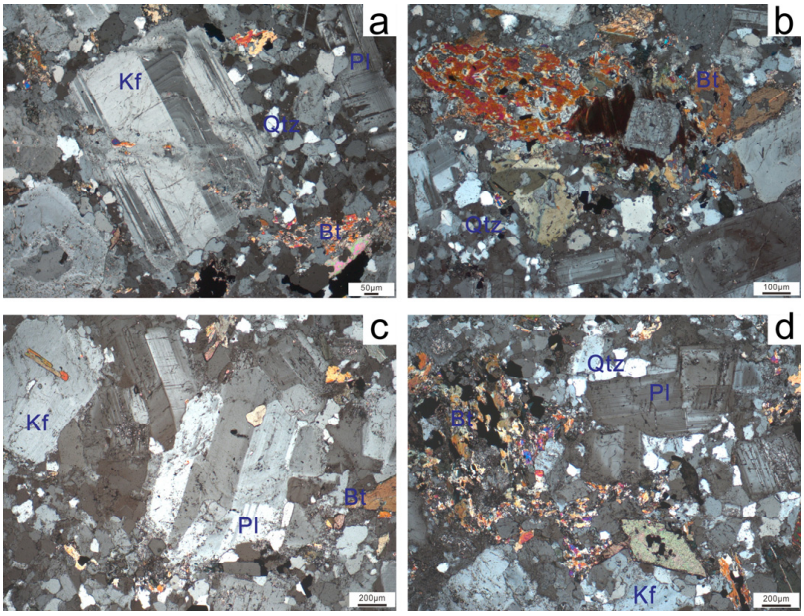

Figure 2. Microphotographs (cross polarized light) of thin sections of the representative adakitic rocks from the drill holes in the DGS deposit. (**a**) tabular K-feldspar (**b**) flaky biotite with polychromatic property (**c**) and (**d**) mineral assemblage of quartz + K-feldspar + plagioclase + biotite. Abbreviations in the images: Kf = potassium feldspar; Pl = plagioclase; Qtz = quartz; Bt = biotite.

3. Analytical Methods

3.1. In Situ SIMS Zircon U–Pb and Oxygen Isotope Analysis

Zircon grains were separated and mounted in epoxy resin disc with standards Plešovice, Penglai, and Qinghu and then polished to expose the crystals. The U–Pb isotope compositions of zircon grains from sample (DGS46) were determined using a Cameca IMS-1280 HR (high-resolution) at the Guangzhou Institute of Geochemistry, Chinese Academy of Sciences (GIGCAS), Guangzhou, China. The operating conditions include ~8 nA primary O^{2-} beam focused to a beam size of 20 × 30 μm at a mass resolving power of ~5400. U–Pb ratios were calibrated against the Plešovice standard ($^{206}Pb/^{238}U$ = 0.05369; age = 337.1 Ma; [52]), and absolute abundances were determined relative to the M257 standard (U = 840 ppm; Th/U = 0.27; [53]). Zricon standard Qinghu was analyzed together with the zircons in this study. The analytical procedures and data-processing procedures were similar to those described by Li et al. [54]. An average present-day crustal composition [55] was used. The concordia plot was processed using Isoplot/Ex v.3.70 [56]. In situ zircon U–Pb dating results are listed in Supplementary Table S1. The analysis shows that $^{206}Pb/^{204}Pb$ values are generally high, implying insignificant common Pb contents.

Zircon oxygen isotopes (^{18}O and ^{16}O) were determined using a Cameca IMS-1280 HR ion microprobe at the GIGCAS. The sample mount was reground and polished. A focused beam of Cs^+ ions was accelerated at 10 kV potential with an intensity of ~2nA. The applied beam diameter was ~20 μm. The oxygen isotopes were measured in multi-collection mode using two off-axis Faraday cups, and nuclear magnetic resonance (NMR) was used to stabilize the magnetic field. Detailed analytical procedures were described by Tang et al. [57]. Each analysis comprised 20 cycles, with an internal precision of better than 0.2‰ (1σ). Measured ^{18}O and ^{16}O were normalized to the Vienna Standard Mean Ocean Water composition (VSMOW; $^{18}O/^{16}O$ = 0.0020052) and reported in standard per mil notation. The instrumental mass fraction factor (IMF) was corrected using the zircon standard Penglai with $\delta^{18}O_{VSMOW}$ = 5.3‰ [58]. In situ oxygen isotopic results are presented in Supplementary Table S2.

3.2. Whole-Rock Major and Trace Elements and Sr–Nd Isotopes

Rock samples were crushed to smaller than 200 mesh (<0.75 μm in diameter). The powder samples were dried at 105 °C for 4 h and treated to produce fused glass discs that were analyzed using an X-ray fluorescence spectrometer at ALS Laboratory Group, Analytical Chemistry and Testing Services, Guangzhou, China. The analytical uncertainties for major element concentrations were less than 5%. Whole-rock trace element analyses were conducted using an Agilent 7700e inductively coupled plasma–mass spectrometer (ICP–MS) at Wuhan SampleSolution Analytical Technology, Wuhan, China. The sample digestion procedure and the analytical precision and accuracy during ICP–MS analyses were identical to those of Liu et al. [59]. The instrumental signal drift was monitored using an internal standard Rh solution. The AGV-2, BHVO-2, BCR-2, and RGM-2 standards were used for instrument calibration and quality control. For most trace and rare earth elements, the precision was estimated to be better than 2%–5% RSD (relative standard deviation). The data are given in Supplementary Table S3.

Strontium and Nd isotopic compositions of the powdered samples were determined using a Micromass Isoprobe multi-collector ICP–MS instrument (MC–ICP–MS) at the State Key Laboratory of Isotope Geochemistry, GIGCAS. The powder samples were dissolved in HF + HNO_3 acid in Teflon containers. Strontium and rare earth elements (REE) were separated in cation columns, Nd fractions were further separated using HDEHP-coated Kef columns. Analytical procedures were similar to those described by Li et al. [60]. The MC–ICP–MS was operated in static mode. The measured $^{87}Sr/^{86}Sr$ of the NBS SRM 987 standard and the measured $^{143}Nd/^{144}Nd$ of the Shin Etsu JNdi-1 standard yielded the values of 0.710242 ± 10 (2σ, n = 9) and 0.512115 ± 10 (2σ, n = 8), respectively, which were identical within the error of the recommended values of $^{87}Sr/^{86}Sr$ = 0.71025 and $^{143}Nd/^{144}Nd$ = 0.512115 [61]. To correct for mass fractionation during analysis, measured Sr and Nd isotope ratios were normalized to a composition of $^{86}Sr/^{88}Sr$ = 0.1194 and $^{146}Nd/^{144}Nd$ = 0.7219. Isotopic compositions and calculated initial $^{87}Sr/^{86}Sr$ (I_{Sr}) and ε_{Nd} (t) values are shown in Supplementary Table S3.

3.3. Apatite Major Elements Analysis

Apatite grains from the sample (DGS46) were separated and selectively mounted in epoxy resin and then polished to expose crystal mid-sections for observation and analysis. Photomicrographs and cathodoluminescence (CL) images were obtained to characterize the internal structures of apatite grains. Major element analyses were conducted using wavelength-dispersive spectrometers on a JEOL JXA-8230 electron microprobe at the Testing Center of the Shandong office of the China Metallurgical Geology Bureau, Jinan, China. The operating conditions include an accelerating voltage of 15 kV, a beam current of 10 nA, and a defocused beam 10 μm in diameter. Norbergite standard was used for F, $Ba_5(PO_4)_3Cl$ for Cl, and apatite for Ca and P contents. In order to avoid volatile loss, count times analyzed for F and Cl were 10 s and was 20 s for other elements. Fluorine and Cl were analyzed using the Kα line on an LDE1 and PET crystal, respectively. The analytical precision was estimated to be better than 1% for most of the major elements and was ~5% for F and Cl contents. The major element contents of apatite are listed in Supplementary Table S4.

4. Results

4.1. Zircon U-Pb Age and O Isotopic Compositions

Zircon grains from quartz monzodiorite (DGS46) are transparent and colorless. Most crystals are euhedral to subhedral in morphology. The selected grains have lengths up to 100–300 μm, with length-to-width ratios between 2:1 and 3:1. They are all characterized by euhedral concentric zoning in CL images, indicating their magmatic origin. A total of 16 U-Th-Pb measurements on 16 zircons yielded moderate concentrations of Th (70–536 ppm) and U (98–695 ppm), with variable Th/U ratios ranging from 0.34 to 1.02. Only one inherited zircon crystal showed an age of 829 Ma. The other 15 points define a concordia

age of 138.9 ± 1.8 Ma (n = 15, MSWD = 0.77) (Figure 3), which is considered to be the best estimate of the crystallization age of the DGS intrusion.

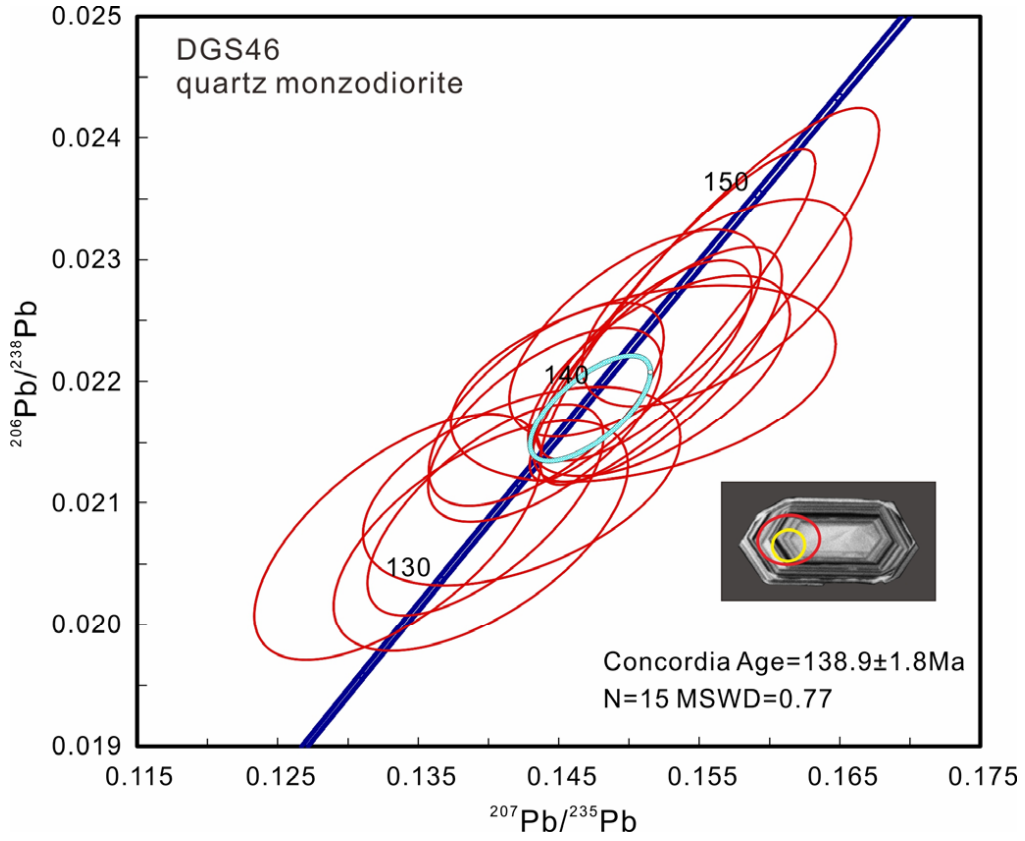

Figure 3. SIMS zircon U-Pb Concordia diagram for the DGS quartz monzodiorite. The inset shows representative CL image of the investigated zircon grain, with locations of ion microprobe analysis spots (yellow circle represents the spot of O isotope, and red oval represents U–Pb dating analyses).

Oxygen isotope analyses on the dated zircon grains from sample DGS46 yielded a relatively wide range of $\delta^{18}O$ values (5.7‰ to 7.3‰), with one xenocrystic zircon crystal showing a $\delta^{18}O$ value of 5.6‰. Taking into account the SiO_2 contents of the host rock and using the equation $\delta^{18}O_{WR} \approx \delta^{18}O_{Zir}$ + 0.0612 (wt% SiO_2) −2.5 [35], the corresponding $\delta^{18}O$ values for the quartz monzodiorite were calculated at 7.3‰–8.8‰.

4.2. Whole-Rock Major and Trace Elements and Sr-Nd Isotope

The quartz monzodiorites contain 63.2–67.9 wt% SiO_2, 14.9–16.2 wt% Al_2O_3, and 5.86–8.02 wt% total alkalies contents, with Na_2O/K_2O ratios from 1.48 to 1.71 (Figure 4). These samples fall into the metaluminous field in the A/CNK-A/NK diagram (Figure 4). In the K_2O vs. SiO_2 diagram, the samples are mainly plotted in the high-K calc-alkaline series and exhibit a strong positive correlation between K_2O and SiO_2 (Figure 5e). Significantly negative correlations exist between the SiO_2 content and TiO_2, MgO, CaO, and P_2O_5 content.

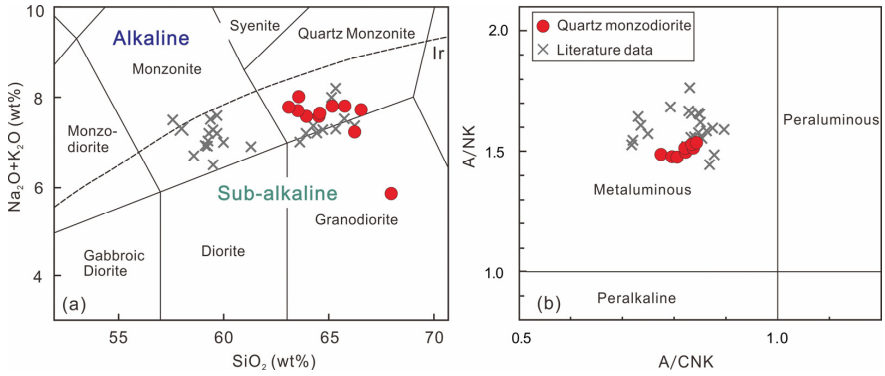

Figure 4. Classification diagrams of DGS quartz monzodiorite. (**a**) TAS diagram of DGS quartz monzodiorite [62]. (**b**) A/NK versus A/CNK diagram for DGS quartz monzodiorite. A/NK = Al/(Na + K), A/CNK = Al/(Ca + Na + K) (molar ratios). Literature data of adakitic rocks in the DGS deposit are from the following references: Wang et al. [11] and Wang et al. [63].

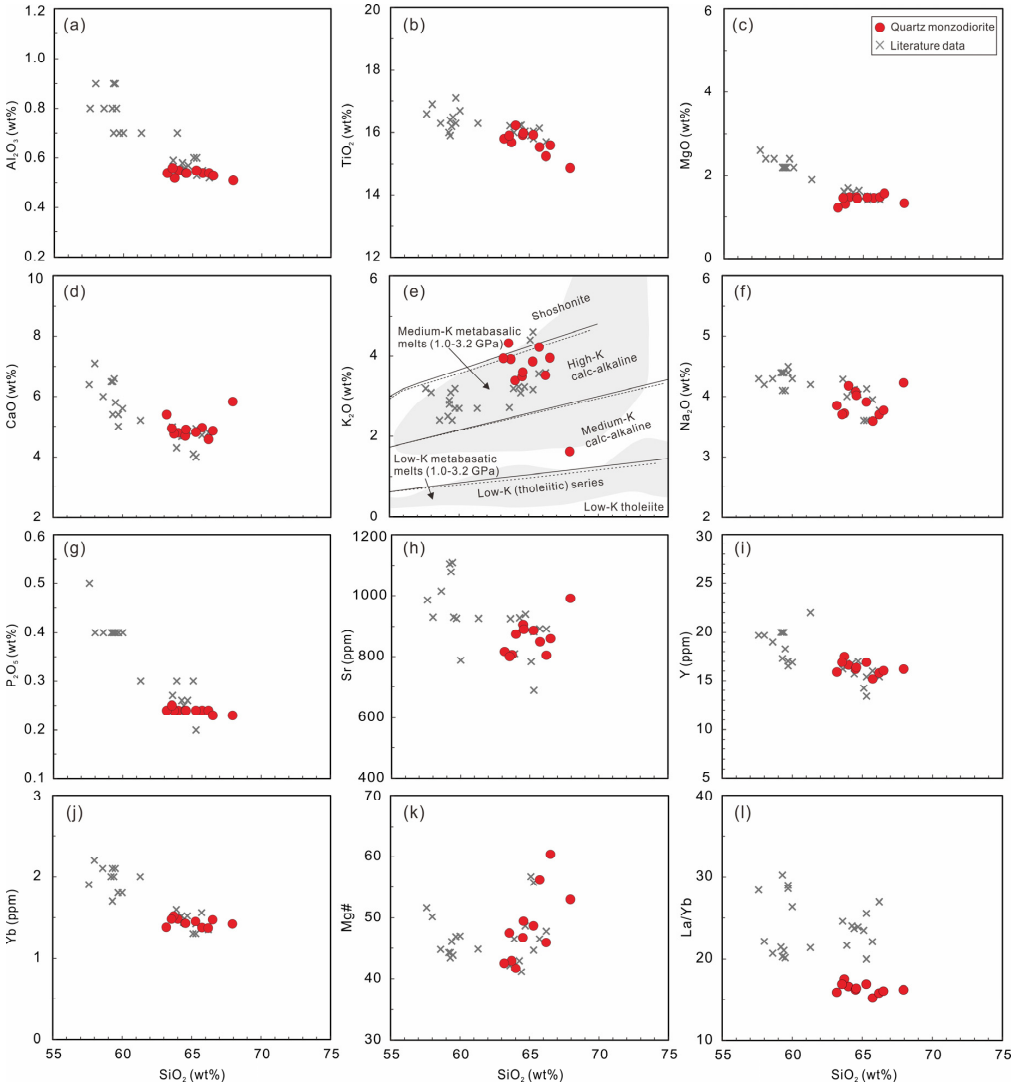

Figure 5. Harker diagrams of DGS quartz monzodiorite. (**a**) Al_2O_3 vs. SiO_2; (**b**) TiO_2 vs. SiO_2; (**c**) MgO vs. SiO_2; (**d**) CaO vs. SiO_2; (**e**) K_2O vs. SiO_2; (**f**) Na_2O vs. SiO_2; (**g**) P_2O_5 vs. SiO_2; (**h**) Sr vs. SiO_2; (**h**) Sr vs. SiO_2; (**i**) Y vs. SiO_2; (**j**) Yb vs. SiO_2; (**k**) Mg# vs. SiO_2; (**l**) La/Yb vs. SiO_2. Literature data are from Wang et al. [11] and Wang et al. [63].

The chondrite-normalized REE patterns of the quartz monzodiorite (Figure 6a) are characterized by moderate to high LREE enrichment relative to HREE [$(La/Yb)_N$ ratios > 14.6] and pronounced negative Eu anomalies (Eu/Eu* = 0.30−0.34). The primitive mantle-normalized trace element patterns are shown in Figure 6b. The quartz monzodiorites are characterized by high Ba (588–1040 ppm), Sr (800–991 ppm), and LREE contents, as well as low Rb (44.3–111 ppm) and HREE contents. The quartz monzodiorite shows enrichment in LILE (Rb and Pb) and depletion in HFSE. The concentrations of HFSE are relatively low, with Zr ranging from 146 to 173 ppm, Nb from 12.3 to 14.3 ppm, Ta from 0.79 to 0.96 ppm, and Y from 15.2 to 17.5 ppm. These geochemical characterizations imply that the formation of the DGS quartz monzodiorite is related to the subduction scenario [64,65].

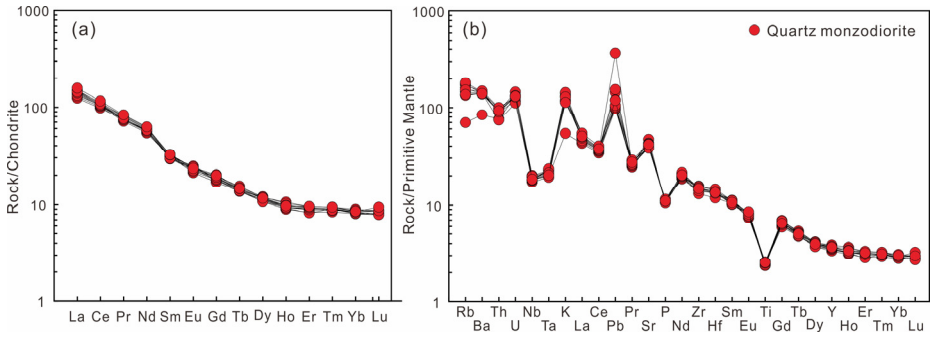

Figure 6. Chondrite-normalized REE (**a**) and primitive mantle-normalized trace elements (**b**) distribution patterns of DGS quartz monzodiorite. Chondrite and primitive mantle-normalized data taken from Sun and McDonough [66].

Two DGS samples (DGS46 and DGS53) were measured for Sr–Nd isotopic compositions. Both Sr and Nd isotopic compositions vary narrowly within a small range (Figure 7). The measured $^{87}Sr/^{86}Sr$ ratios vary between 0.70855 and 0.70856, corresponding to the initial $^{87}Sr/^{86}Sr$ ratio (I_{Sr}) between 0.70783 and 0.70794. $^{147}Sm/^{144}Nd$ vary in a small range (0.0864–0.0995), with $^{143}Nd/^{144}Nd$ ratios and $\varepsilon_{Nd}(t)$ values of 0.51198–0.51199 and −11.0 to −11.1, respectively.

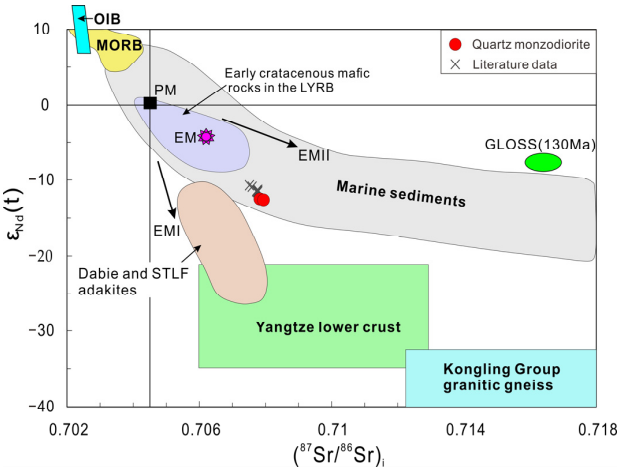

Figure 7. Whole-rock Sr-Nd isotopic compositions of DGS intrusive rocks. The fields of PM (primitive mantle) and MORB are according to Hofmann [67]; the field of GLOSS (global subducting sediment) is based on Plank and Langmuir [68]; the fields of Sr-Nd isotopic compositions for the LYRB Cretaceous mafic rocks, NE Yangtze Block and the Archean Kongling Group metamorphic basement and the Dabie Orogen low-Mg adakitic rocks are after compilation of Liu et al. [13], Li et al. [54], Chen et al. [69], Yan et al. [70] and Ames et al. [71]. Literature data are from Li et al. [54]. Abbreviations in the diagram: EM = Enriched Mantle, EMI = Enriched Mantle I, EMII = Enriched Mantle II, STLF = South Tan-Lu fault.

4.3. Apatite Geochemistry

Most apatite grains from DGS46 quartz monzodiorite are subhedral and euhedral, ~100–300 μm in length with length, with width ratios of 1:1 to 3:1. They are characterized as clean, homogeneous, and transparent under plane-polarized light. The CL images exhibit concentric and oscillatory zoning. All those features are interpreted to be due to the magmatic origin [72]. Euhedral–subhedral apatite grains with no inclusions were selected for analysis. The analyzed apatite grains have CaO content from 54.0 to 55.1 wt% and P_2O_5 in a range of 41.6 to 43.1 wt%. Apatite grains have Na_2O content below 0.06 wt% and SO_3 content ranging from 0.08 to 0.28 wt%. The relatively positive correlation between Na_2O and SO_3 (Figure 8a) reveals that they were incorporated in apatite at the same time via a coupled substitution mechanism (e.g., $SO_4^{2-} + Na^+ = PO_4^{3-} + Ca^{2+}$; [73]). They yielded higher F (1.88–3.16 wt%) compared to Cl (0.06–0.16 wt%) contents (Figure 8b). Assuming that the halogen site is fully occupied by $X_{F\text{-}ap} + X_{Cl\text{-}ap} + X_{OH\text{-}ap} = 1$ (X = mole fractions modal of F, Cl, and OH), the OH content in apatite is calculated via stoichiometry based on eight anions [74]. The calculated OH contents range from 0.09 to 0.45 apfu (Figure 8c).

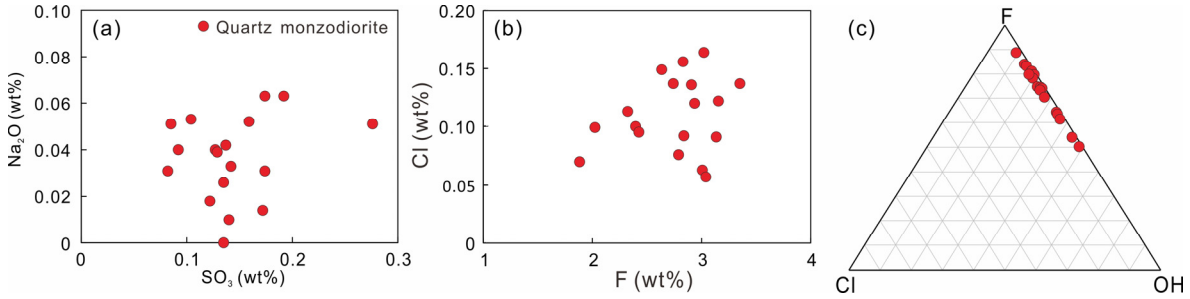

Figure 8. Variation diagrams of major element contents for apatite in the DGS quartz monzodiorite. (**a**) Na_2O (wt%) vs. SO_3 (wt%); (**b**) Cl (wt%) vs. F (wt%); (**c**) F-Cl-OH ternary diagram based on the F-Cl-OH atomic proportions in apatites.

Using the method of Piccoli and Candela [74], the estimated apatite saturation temperature (956 °C; Supplementary Table S4) was attained based on the whole-rock data. Such a high temperature suggests that apatite in the DGS quartz monzodiorite is an early crystallized mineral phase [75]. Moreover, the analyzed apatites are generally ~100–300 μm in length, much larger than the euhedral and fine-grained ones (25 μm) crystallizing from the intercumulus melt but cannot record bulk magma information [76,77]. Considering the apatite morphology and contact relationship, we concluded that apatite grains in the quartz monzodiorite are in the early crystallizing phase and can be used to evaluate the physicochemical conditions of the parental magma.

5. Discussion

5.1. Petrogenesis of the DGS Quartz Monzodiorite

Adakitic rocks have attracted extensive attention worldwide, as they are not only record magmatic processes and mantle–crustal interaction but are also associated with major Cu deposits. The term 'adakite' was initially considered to be partial-melting products of subducted hot, young oceanic crust metamorphosed in the garnet amphibolite or eclogite facies [78]. Adakites are intermediate to felsic igneous rocks characterized by SiO_2 contents (≥56 wt%), high Al_2O_3 contents (≥15 wt%), Sr concentrations (mostly ≥ 400 ppm), and Sr/Y (≥20) ratios but low Y and Yb concentrations (generally ≤18 ppm and ≤1.9 ppm, respectively) and a lack of Eu anomalies [78,79]. The DGS quartz monzodiorites have high SiO_2 and Al_2O_3 contents varying from 63.2 to 67.9 wt% and 14.9 to 16.2 wt%, respectively. They have high Sr (800–991 ppm), low Y (15.2–17.5 ppm) and Yb (1.37–1.52 ppm) concentrations, and resultant high Sr/Y (46–61) and $(La/Yb)_N$ (14.8–18.5) ratios, which are all typical geochemical features of adakites [78]. In the discrimination diagrams (Figure 9), most of the samples fall in or on the boundary of the adakite field.

Due to the importance of understanding the genesis of adakitic rocks, their origin is still hotly debated. In addition to slab melting, an increasing number of studies have proposed alternative processes that could form adakitic magmas in different tectonic backgrounds, not only island arc settings but also intraplate environments [78–84]. The mechanisms that generate adakitic rocks could be summarized as partial melting of thickened or delaminated mafic rocks in the lower continental crust [85–88], garnet or amphibole fractionation under different pressures [89–91], and partial melting of the upper mantle metasomatized by slab-derived melt [92,93]. The sources and genesis of the ore-bearing adakitic rocks in the Tongling ore cluster are still controversial. Previous studies proposed several processes that could generate these adakites, such as partial melting of the subducted Paleo-Pacific oceanic crust or mantle wedge metasomatized by the Paleo-Pacific plate [6–8,13,17,20,21], partial melting of delaminated or thickened lower continental crust [22–25], or mixing of mantle-derived and evolved felsic crust-derived magmas [11,30–34].

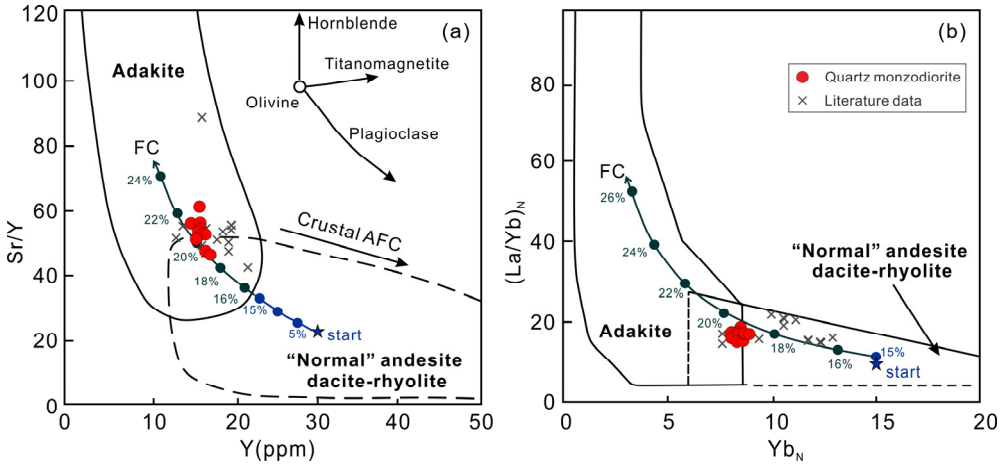

Figure 9. Discrimination diagrams for DGS adakitic rocks. Sr/Y versus Y (**a**) and $(La/Yb)_N$ versus Yb_N (**b**) after Drummond and Defant [78]. A two-stage modeled Rayleigh fractionation from a calc-alkaline andesite melt modeled after Li et al. [94]. Dark-blue line represents the first-stage magmatic fractionation (from andesite to dacite); dark-green line indicates the second-stage magmatic fractionation (from dacite to rhyolite). FC = fractional crystallization, AFC = assimilation and fractional crystallization. Literature data are from Wang et al. [11] and Wang et al. [63].

Adakitic rocks generated from partial melting of the continental or oceanic crust may be distinguished by some geochemical features. Based on these features, the DGS adakitic rocks could not be products of continental crust melting. First, the melts with garnet as the residual mineral in the source area will have high ratios of Yb/Lu (8–10) and a steep HREE distribution pattern [95]. The DGS adakitic rocks have relatively low Yb/Lu ratios (6.0–7.2) and flat HREE distribution patterns, which do not agree with this model. Second, experimental petrology studies suggest that the magma originated from partial melting of the basaltic lower crust and is usually enriched in Na_2O (>4.3 wt%) [85,96]. However, the Na_2O content of DGS adakitic rocks (3.6 to 4.2 wt%) is lower and inconsistent with the model of delaminated or thickened lower continental crust. Moreover, the diagram of Sr/Y versus $(La/Yb)_N$ can also provide information for distinguishing between partial melting from the subducted oceanic slab and lower continental crust [13,20,87]. Under such conditions, in the amphibole- or garnet-bearing and plagioclase-free residues, both Y and Yb are compatible, whereas Sr and La are incompatible. A positive correlation exists between the $(La/Yb)_N$ and Sr/Y ratios in the adakites, which are products of the partial melting of thickened lower continental crust with an eclogite or garnet amphibolite residue. In modern subduction zones, adakites produced by the melting of oceanic crust might have variably high Sr/Y but considerably lower $(La/Yb)_N$ ratios compared to those of the lower continental crust [13,97–99]. The DGS adakitic rocks have high and variable Sr/Y ratios but considerably lower $(La/Yb)_N$ ratios than those derived from the lower

continental crust, and all plot in the field of partial melting of subducting oceanic crust (Figure 9). Therefore, the mechanism of partial melting of the lower continental crust could not explain the genesis of DGS adakitic rocks.

Moreover, fractional crystallization plays an important role in the varied geochemical compositions of the DGS adakitic rocks. The negative correlations observed between P_2O_5, TiO_2, Y, and SiO_2 (Figure 5) imply that the separation of accessory minerals buffering P and Ti leads to decreased REE and Y contents during magmatic evolution. Considering the strong depletion of Nb (Figure 6) and the varied and overall subchondritic Nb/Ta ratios (13.5–16.2), Nb-Ta fractionation might have happened under the geothermal gradient in the incipient stage of subduction [100–103].

Only a few studies have reported the zircon $\delta^{18}O$ values of adakitic rocks in the LYRB. Most zircon $\delta^{18}O$ values vary between 6.5‰ and 8.0‰, corresponding to 8.0‰–9.5‰ for $\delta^{18}O$ values of the ore-bearing magmas (Figure 10). In this study, the zircon $\delta^{18}O$ values of the DGS adakitic rocks were first analyzed and reported as 5.7‰ to 7.3‰, corresponding to 7.3‰ to 8.8‰ for the magma. Considering that only one xenocrystic zircon is found among the dated zircons, contamination of the crustal materials during ascent might be very limited. Therefore, the oxygen isotope is a good indicator of the primitive nature of magmatic sources. The calculated magmatic $\delta^{18}O$ values (7.3‰–8.8‰) are higher than melts from hydrothermally altered gabbros from the oceanic crust interior ($\delta^{18}O$ = ca. 2‰–5‰) but lower than those from partial melting of sediments and/or basaltic rocks in the upper part of the oceanic crust ($\delta^{18}O$ = 9‰–20‰) [104]. In addition to the high and variable oxygen isotopic compositions, the DGS adakitic rocks display rather high initial I_{Sr} (0.70783 to 0.70794) and enriched $\varepsilon_{Nd}(t)$ (−11) values. The Sr-Nd isotopic data for the adakitic rocks in DGS lie in the area among MORB, marine sediment, and the ancient lower crust (Figure 7). All these isotopic features indicate the progressive addition of ancient crustal materials in the magma source. These materials could be the subducted sediments involved in the magma source during slab melting or continental crust materials incorporated through magma mixing or crustal contamination. Therefore, the integrated higher $\delta^{18}O$ and I_{Sr} values and lower ε_{Nd} (t) values of the DGS adakitic rocks can be attributed to the mantle source involved in a fraction of sedimentary melts, whereas the crustal contamination had little role, if any, in their genesis.

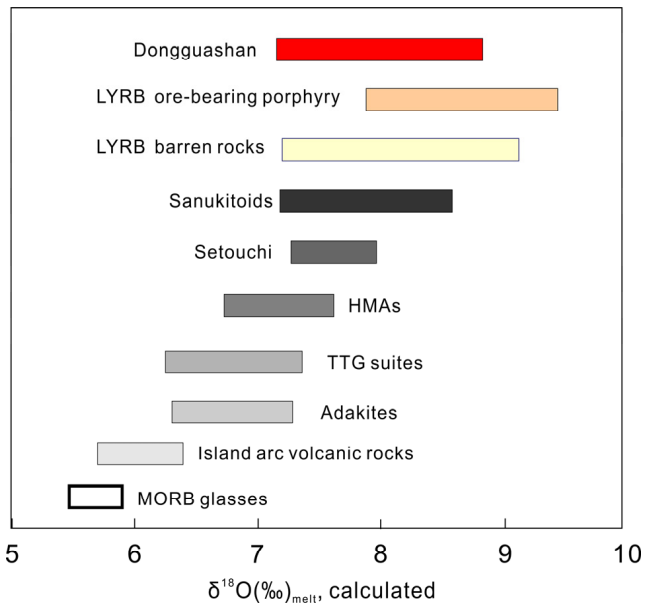

Figure 10. Magmatic $\delta^{18}O$ values of the DGS adakitic rocks and LYRB adakitic rocks, normal island arc volcanic rocks and other high Sr/Y rocks. The figure is modified after Li et al. [94]. Data sources are after compilation by Li et al. [94] and Bindeman et al. [104].

5.2. Temporal Relationship between the Adakitic Rocks and Cu polymetallic Mineralization in the DGS Deposit

Given the Late Mesozoic magmatic activities in the LYRB, adakitic rocks developed at ca. 150–130 Ma have been tightly associated with intense Cu-Au-Mo-Fe mineralization [7,13,15,17]. Previous geochronological studies on the DGS deposit mainly focused on the mineralization ages, including the mineralized quartz veins Rb-Sr age (~136 Ma; [105]), molybdenite Re-Os age (~139 Ma; [106]), garnet U-Pb ages (from ~135 to 136 Ma; [107]), and titanite U-Pb ages (from ~139 to 137 Ma; [108]). There are also some crystallization ages of the ore-related pluton, with zircon U-Pb dating results varying between ~135 Ma and ~140 Ma [11,29,45,108,109].

In this study, our new zircon U-Pb dating result is 138.8 ± 1.8 Ma for magmatic zircons from the DGS quartz monzodiorite, which directly constrained the timing of ore-related adakitic rocks and agreed well with previously published ages for the DGS deposit. Therefore, DGS Cu mineralization is temporally related to the adakitic rocks at ~140 Ma –135 Ma from the period of intense Cu-Au-Mo-Fe mineralization in the LYRB.

5.3. Metallogenic Implications for the Cretaceous Adakites in the LYRB

The adakites produced via partial melting of the subducted oceanic slab have a genetic association with Cu mineralization worldwide. The high initial Cu contents of the magmas generated from the oceanic crust are an important parameter that makes the slab melt the best candidate for Cu mineralization [13,21,82,83,98]. The Cu concentration of MORB is ~100 ppm, which is much higher than that of the primitive mantle and the continental crust [99]. The spider diagram of bulk continental crust-normalized transitional elements (Figure 11) shows strong fractionation of DGS adakitic rocks compared to the continental crust, with pronounced positive Cu anomalies and strong depletion of mantle compatible elements (Sc, Cr, and Ni). Moreover, the contents of ore-forming element Cu in the DGS samples reach up to 227 ppm, with an average of 166 ppm, significantly higher than Cu in the bulk continental crust (27 ppm; [99]). The relative enrichment in Cu in the quartz monzodiorite indicates the potential to provide ore-forming materials and the genetic relationship of Cu mineralization with adakites in the DGS deposit.

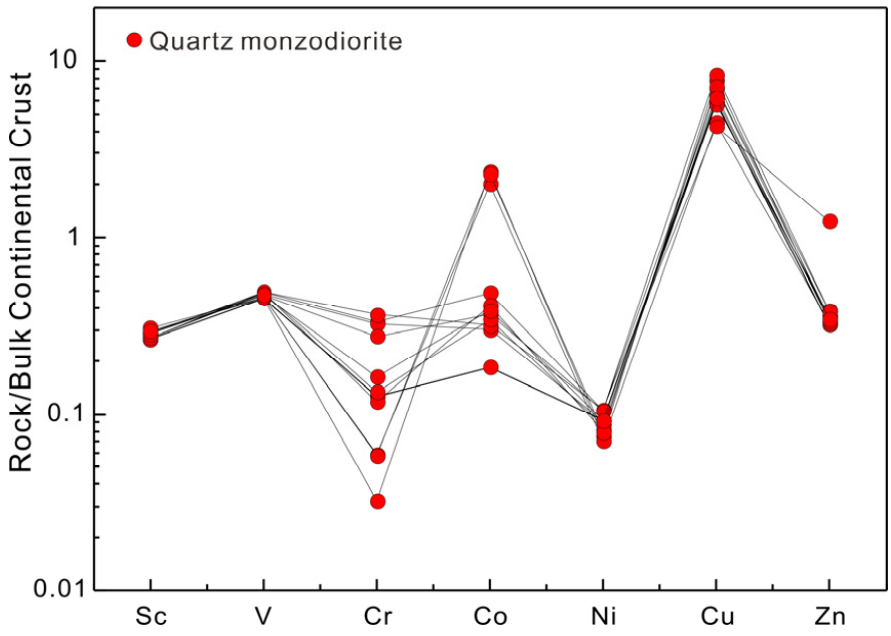

Figure 11. Transitional elements diagram for the DGS adakites. Bulk continental crust compositions are after Rudnick and Gao [99].

The association between Cu deposits and adakitic intrusions in subduction zones suggests that magma oxygen fugacity controls the partitioning and transport of Cu in magmas before mineralization [81,110–113]. Copper is a highly chalcophile element and is enriched in sulfides. The oxygen fugacity controls the sulfur species, and the stability of sulfides controls the Cu partitioning in magmas. During partial melting, high oxygen fugacity is favorable for the liberation of Cu when sulfur is extracted as sulfate and during the enrichment in Cu in the melt during differentiation before partitioning into an exsolved fluids phase [110,114–116].

As apatite is an early-stage crystallization product, it can provide records of the oxidation states of the host magma [75–77,117]. The Mn concentration of apatite is used to determine the redox conditions of granitic magmas due to the increasing concentration with decreasing magma oxygen fugacity (f_{O2}) (e.g., [73,118–120]). Accordingly, Miles et al. [119] proposed that the Mn concentration can be used to calculate oxygen fugacity and is shown to vary linearly and negatively with logf_{O2}, which can be illustrated by the equation logf_{O2} = –0.0022 (± 0.0003) Mn (ppm) − 9.75 (± 0.46). Apatite grains in this study have MnO contents of 0.03–0.12 wt.%, which yield logf_{O2} values from −9.8 to −11.8. Besides, the valence state of sulfur in apatite is controlled by oxygen fugacity [121,122]. Based on the equilibration experiment, a recent study proposed the following equation to estimate oxygen fugacity: ΔFMQ = 0.423 (±0.034) − 0.2 (±0.026) × ln[(0.964 (± 0.001) − 0.086 (±0.033))/($S^{6+}/\Sigma S_{measured}$ − 0.086 (±0.033)) − 1] [121]. Sulfur in apatite is assumed to exist only as S^{2+} and S^{6+}, and the $S^{6+}/\Sigma S$ ratio was estimated according to Wang et al. [75] (S^{6+} content in apatite was obtained by EPMA apatite S content with the subtraction of 36.88 ppm). According to the equation [121], the regional magmatic oxygen fugacities are calculated to be ΔFMQ + 0.89 to ΔFMQ + 1.28 (Supplementary Table S4), representing the lower bound. The oxygen fugacities estimated by Mn (log f_{O2} from −9.8 to −11.8) and S (ΔFMQ + 0.89 to ΔFMQ + 1.28) contents of the apatites indicate that the DGS Cu ore-bearing adakitic magmas are generated in an oxidized environment.

Volatiles play an important role in magmatic evolution and metal enrichment and mineralization [123,124]. Apatite is the main accessory mineral for buffering volatiles (F, Cl, and OH) in magmatic rocks [125,126]. Boyce and Hervig [127] found that variations in F and OH contents in apatite are in line with F and H_2O change in the coexisting melt inclusion. The OH concentration of apatite can reflect the abundance of H_2O in the melt where the apatite crystallized [128–130]. The relatively high OH content contained by apatite grains from the DGS quartz monzodiorite (Figure 8) might indicate high water content of the parental magma. Fluorine and Cl are important for mineralization due to their great significance in depolymerizing the melt structure and facilitating hydrothermal metal transport and enrichment during degassing and exsolution of the fluid phase [38,131,132]. As Cu is more sensitive to Cl than F and the increase in Cl content will markedly increase the solubility of Cu, Cl-rich fluids are essential for the transportation and deposition of Cu [133–135]. The studied apatite grains have high F (1.88–3.35 wt%) and low Cl (0.06–0.16 wt%) contents (Figure 8), with lower Cl/F ratios (0.01 to 0.06). The mantle usually has low Cl contents (<0.1 wt%) and is not significantly influenced by Cl recycling [136]. Magmas are derived from anatexis of the continental crust, which have low Cl/F ratio [124]. Apatite crystallized from the supracrustal material also has low Cl content [137]. The Cl content and Cl/F ratio of apatite grains preclude the generation from mantle-derived magma or supracrustal components. However, Cl is highly incompatible and preferentially enters the liquid phase in the stage of slab dehydration [138]. Comparing our results with apatite from Late Mesozoic granodiorite and polymetallic mineralization in southern Anhui Province, which are identified as fluorapatite with high F (2.69–4.13 wt%) and low Cl contents (mainly < 0.2 wt%) [17,124], slab-derived components with high Cl/F ratios might be incorporated into the formation of adakitic rocks in the DGS deposit.

To summarize, the high Cu content, high oxygen fugacity and volatile-rich adakitic magmas benefit the extraction and transportation of Cu, which finally formed the DGS Cu polymetallic deposits [13,17,81,111,112]. Based on the analysis of previous studies,

we suggest that the diagenesis of Cretaceous adakitic rocks and mineralization of the DGS deposit are the same as other large-scale Cu polymetallic deposits in the LYRB. The hydrous and oxidized subducted altered oceanic crust is potentially favorable for Cu–Au mineralization [17].

6. Conclusions

Based on zircon in situ U–Pb geochronology and O isotope, as well as bulk rock major and trace element and Sr–Nd isotopic compositions of the DGS adakitic rocks associated with the Cu polymetallic deposit in the Tongling ore cluster, LYRB, the following conclusions are drawn:

(1) The DGS intrusion mainly consists of quartz monzodiorite. The whole-rock compositions show geochemical features of adakite, characterized by high Sr and low Y and Yb concentrations and, consequently, high Sr/Y and $(La/Yb)_N$ ratios. According to the comprehensive geochemical data, the adakites are most probably produced by the partial melting of a subducted altered oceanic crust and possibly incorporated sediments.
(2) Highly precise and accurate SIMS in situ zircon U–Pb age suggests that the adakites crystallized at 138.9 ± 1.8 Ma, which is coeval with the Cu mineralization in the DGS deposit, Tongling ore cluster, and implies a close temporal relationship between the adakites and Cu polymetallic mineralization in the LYRB.
(3) The high Cu content, high oxygen fugacity, and volatile contents of the DGS adakite imply an oxidized and volatile enriched environment, which is conducive to the formation of large-scale Cu polymetallic mineralization.

Supplementary Materials: The following supporting information can be downloaded at: https://www.mdpi.com/article/10.3390/min13070953/s1, Figure S1: Photographs of DGS adakitic rocks from drill holes in the DGS deposit; Table S1: SIMS U-Pb zircon age data of adakitic rocks in the DGS deposit; Table S2: In situ zircon oxygen isotopic compositions of adakitic rocks in the DGS deposit; Table S3: Whole-rock major and trace element data and Sr-Nd isotopic compositions of adakitic rocks in the DGS deposit; Table S4: Major element compositions of apatite from the adakite in the DGS deposit.

Author Contributions: Conceptualization, X.J.; methodology, Z.Z. and K.J.; software, X.J.; validation, J.G.; formal analysis, X.J. and K.J.; investigation, X.J.; resources, X.J.; data curation, X.J. and K.J.; writing—original draft preparation, Z.Z.; writing—review and editing, X.J. and J.G.; visualization, Z.Z. and K.J.; supervision, X.J.; project administration, X.J.; funding acquisition, X.J. and Z.Z. All authors have read and agreed to the published version of the manuscript.

Funding: This research was funded by the Guizhou Provincial Science and Technology Projects, (No. ZK[2021] 207 and No. ZK[2023] 052), the CAS 'Light of West China' Program, and the Natural resources Science and Technology Project of Anhui Province (No. 2022-K-9), and a special fund managed by the State Key Laboratory of Ore Deposit Geochemistry, Institute of Geochemistry, Chinese Academy of Sciences.

Data Availability Statement: The original contributions presented in the study are included in the Supplementary Materials.

Acknowledgments: Zhekun Zhang and Saijun Sun are acknowledged for help during the fieldwork. We thank Peijun Lin, Yanqiang Zhang, Boqin Xiong, and Qin Yang for technical assistance with experimental works.

Conflicts of Interest: The authors declare no conflict of interest.

References

1. Chang, Y.F.; Liu, X.P.; Wu, Y.C. *The Copper-Iron Belt of the Lower and Middle Districts of the Yangtze River*; Geological Publishing House: Beijing, China, 1991; pp. 1–379. (In Chinese)
2. Pan, Y.M.; Dong, P. The Lower Changjiang (Yangzi/Yangtze River) metallogenic belt, east central China: Intrusion- and wall rock-hosted Cu-Fe-Au, Mo, Zn, Pb, Ag deposits. *Ore Geol. Rev.* **1999**, *15*, 177–242. [CrossRef]

3. Zhai, Y.S.; Xiong, Y.L.; Yao, S.Z.; Lin, X.D. Metallogeny of copper and iron deposits in the Eastern Yangtze Craton, east-central China. *Ore Geol. Rev.* **1996**, *11*, 229–248. [CrossRef]
4. Mao, J.W.; Xie, G.Q.; Duan, C.; Pirajno, F.; Ishiyama, D.; Chen, Y.C. A tectono-genetic model for porphyry-skarn-stratabound Cu-Au-Mo-Fe and magnetite-apatite deposits along the Middle-Lower Yangtze River valley, Eastern China. *Ore Geol. Rev.* **2011**, *43*, 294–314. [CrossRef]
5. Zhou, T.F.; Wang, S.W.; Fan, Y.; Yuan, F.; Zhang, D.Y.; White, N.C. A review of the intracontinental porphyry deposits in the Middle-Lower Yangtze River Valley metallogenic belt, Eastern China. *Ore Geol. Rev.* **2015**, *65*, 433–456. [CrossRef]
6. Ling, M.X.; Wang, F.Y.; Ding, X.; Hu, Y.H.; Zhou, J.B.; Zartman, R.E.; Yang, X.Y.; Sun, W.D. Cretaceous ridge subduction along the lower Yangtze River Belt, Eastern China. *Econ. Geol.* **2009**, *104*, 303–321. [CrossRef]
7. Xie, J.C.; Wang, Y.; Li, Q.Z.; Yan, J.; Sun, W.D. Petrogenesis and metallogenic implications of Late Mesozoic intrusive rocks in the Tongling region, eastern China: A case study and perspective review. *Int. Geol. Rev.* **2018**, *60*, 1361–1380. [CrossRef]
8. Xie, J.C.; Tang, D.W.; Xia, D.M.; Wang, Y.; Li, Q.Z.; Yan, J.; Yang, X.Y.; Sun, W.D. Geochronological and geochemical constraints on the formation of Chizhou Cu-Mo polymetallic deposits, middle and lower Yangtze metallogenic belt, eastern China. *Ore Geol. Rev.* **2019**, *109*, 322–347. [CrossRef]
9. Tang, Y.C.; Wu, Y.C.; Chu, G.Z.; Xing, F.M.; Wang, Y.M.; Cao, F.Y.; Chang, Y.F. *Geology of Copper-Gold Polymetallic Deposits in the Along-Changjiang Area of Anhui Province*; Geological Publishing House: Beijing, China, 1998; pp. 1–351. (In Chinese)
10. Zhao, Y.M.; Zhang, Y.N.; Bi, C.S. Geology of gold-bearing skarn deposits in the middle and lower Yangtze River Valley and adjacent regions. *Ore Geol. Rev.* **1999**, *14*, 227–249. [CrossRef]
11. Wang, S.W.; Zhou, T.F.; Yuan, F.; Fan, Y.; Zhang, L.J.; Song, Y.L. Petrogenesis of Dongguashan skarn-porphyry Cu-Au deposit related intrusion in the Tongling district, eastern China: Geochronological, mineralogical, geochemical and Hf isotopic evidence. *Ore Geol. Rev.* **2015**, *64*, 53–70. [CrossRef]
12. Mao, J.W.; Wang, Y.T.; Lehmann, B.; Yu, J.J.; Du, A.D.; Mei, Y.X.; Li, Y.F.; Zang, W.S.; Stein, H.J.; Zhou, T.F. Molybdenite Re-Os and albite 40Ar/39Ar dating of Cu-Au-Mo and magnetite porphyry systems in the Yangtze River valley and metallogenic implications. *Ore Geol. Rev.* **2006**, *29*, 307–324. [CrossRef]
13. Liu, S.A.; Li, S.G.; He, Y.S.; Huang, F. Geochemical contrasts between early Cretaceous ore-bearing and ore barren high-Mg adakites in central-eastern China: Implications for petrogenesis and Cu-Au mineralization. *Geochim. Cosmochim. Acta* **2010**, *74*, 7160–7178. [CrossRef]
14. Yan, J.; Liu, J.M.; Li, Q.Z.; Xing, G.F.; Liu, X.Q.; Xie, J.C.; Chu, X.Q.; Chen, Z.F. In situ zircon Hf-O isotopic analyses of late Mesozoic magmatic rocks in the Lower Yangtze River Belt, central eastern China: Implications for petrogenesis and geodynamic evolution. *Lithos* **2015**, *227*, 57–76. [CrossRef]
15. Xie, J.C.; Wang, Y.; Li, Q.Z.; Liu, J.M.; Yan, J.; Sun, W.D. Early Cretaceous adakitic rocks in the Anqing region, southeastern China: Constraints on petrogenesis and metallogenic significance. *Int. Geol. Rev.* **2017**, *60*, 1362672. [CrossRef]
16. Jiang, X.Y.; Ling, M.X.; Wu, K.; Zhang, Z.K.; Sui, Q.L.; Sun, W.D.; Xia, X.P. Insights into the origin of coexisting A1– And A2–Type granites: Implications from zircon Hf-O isotopes of the Huayuangong intrusion in the Lower Yangtze River Belt, eastern China. *Lithos* **2018**, *318–319*, 230–243. [CrossRef]
17. Jiang, X.Y.; Deng, J.H.; Luo, J.C.; Zhang, L.P.; Luo, Z.B.; Yan, H.B.; Sun, W.D. Petrogenesis of Early Cretaceous adakites in Tongguanshan Cu–Au polymetallic deposit, Tongling region, Eastern China. *Ore Geol. Rev.* **2020**, *126*, 103717. [CrossRef]
18. Jiang, X.Y.; Zhang, Z.Z.; Luo, J.C.; Wei, L.M.; Jiang, K.N. Two-stage, U-mineralization of A-type granites from the Huangmeijian complex, eastern China. *Solid Earth Sci.* **2023**, *8*, 12–24. [CrossRef]
19. Zhu, Z.Y.; Jiang, S.Y.; Hu, J.; Gu, L.X.; Li, J. Geochronology, geochemistry, and mineralization of the granodiorite porphyry hosting the Matou Cu–Mo (±W) deposit, Lower Yangtze River metallogenic belt, eastern China. *J. Asian Earth Sci.* **2014**, *79*, 623–640. [CrossRef]
20. Ling, M.X.; Wang, F.Y.; Ding, X.; Zhou, J.B.; Sun, W.D. Different origins of adakites from the Dabie Mountains and the Lower Yangtze River belt in eastern China, Geochemical constraints. *Int. Geol. Rev.* **2011**, *53*, 727–740. [CrossRef]
21. Sun, W.D.; Ling, M.X.; Yang, X.Y. Ridge subduction and porphyry copper gold mineralization: An overview. *Sci. China Earth Sci.* **2010**, *53*, 475–484. [CrossRef]
22. Zhang, Q.; Wang, Y.; Wang, Y.L. Preliminary study on the components of the lower crust in east China Plateau during Yanshan Period: Constraints on Sr and Nd isotopic compositions of adakite-like rocks. *Acta Petrol. Sin.* **2001**, *17*, 505–513, (In Chinese with English Abstract).
23. Wang, Q.; Zhao, Z.H.; Xu, J.F.; Li, X.H.; Xiong, X.L.; Bao, Z.W. Petrogenesis of the Mesozoic intrusive rocks in the Tongling area, Anhui Province, China and their constraint on geodynamic process. *Sci. China. Ser. D Earth Sci.* **2003**, *46*, 801–815. [CrossRef]
24. Wang, Q.; Xu, J.F.; Zhao, Z.H.; Xiong, X.L.; Bao, Z.W.; Li, C.F.; Bai, Z.H. Petrogenesis of Cretaceous adakitic and shoshonitic igneous rocks in the Luzong area, Anhui Province (eastern China), Implications for geodynamics and Cu-Au mineralization. *Lithos* **2006**, *89*, 424–446. [CrossRef]
25. Wang, Y.; Deng, J.F.; Ji, G.Y. A perspective on the geotectonic of early Cretaceous adakite-like rocks in the lower reaches of Yangtze River and its significance for copper-gold mineralization. *Acta Petrol. Sin.* **2004**, *20*, 297–314, (In Chinese with English Abstract).
26. Deng, J.F.; Wu, Z.X. Lithospheric thinning event in the Lower Yangtze craton and Cu-Fe metallogenic belt in the middle and Lower Yangtze River reaches. *Geol. Anhui* **2001**, *11*, 86–91, (In Chinese with English Abstract).

27. Qin, X.L. Studies on Sulfi-Metal Oxide Inclusions from Mesozoic Intrusions and Their Rock xenoliths in Tongling, Anhui Province. Ph.D. Thesis, China University of Geosciences, Beijing, China, 2007; pp. 1–170, (In Chinese with English Abstract).
28. Yang, X.N.; Xu, Z.W.; Lu, X.C.; Jiang, S.Y.; Ling, H.F.; Liu, L.G.; Chen, D.Y. Porphyry and skarn Au-Cu deposits in the Shizishan orefield, Tongling, East China, U-Pb dating and in-situ Hf isotope analysis of zircons and petrogenesis of associated granitoids. *Ore Geol. Rev.* **2011**, *43*, 182–193. [CrossRef]
29. Guo, W.M.; Lu, J.J.; Jiang, S.Y.; Zhang, R.Q.; Zhao, Z.J. Chronology, Hf isotopes, geochemistry, and petrogenesis of the magmatic rocks in the Shizishan ore field of Tongling, Anhui Province. *Sci. China Earth Sci.* **2013**, *8*, 1268–1286, (In Chinese with English Abstract). [CrossRef]
30. Di, Y.; Zhao, H.; Zhang, Y.; Zhao, J.; Yang, L. Petrographic evidences for magma mixing in the granitoids from Tongling area, Anhui Province. *Beijing Geol.* **2003**, *15*, 12–17, (In Chinese with English Abstract).
31. Wu, C.L.; Chen, S.Y.; Shi, R.D.; Hao, M.Y. Origin and features of the Mesozoic intermediate-acid intrusive in the Tongling area, Anhui, China. *Acta Geosci. Sin.* **2003**, *24*, 41–48, (In Chinese with English Abstract).
32. Wu, C.L.; Dong, S.W.; Gou, H.P.; Guo, X.Y.; Gao, Q.M.; Liu, L.G.; Chen, Q.L.; Lei, M.; Wooden, J.L.; Mazadab, F.K.; et al. Zircon SHRIMP U-Pb dating of intermediate-acid intrusive rocks from Shizishan, Tongling and magmatism. *Acta Petrol. Sin.* **2008**, *24*, 1801–1812, (In Chinese with English Abstract).
33. Xu, J.H.; Xie, Y.L.; Yang, Z.S.; Meng, Y.F.; Zeng, P.S. Trace elements in fluid inclusions of submarine exhalation-sedimentation system in Tongling metallogenic province. *Miner. Depos.* **2004**, *23*, 344–352, (In Chinese with English Abstract).
34. Du, Y.; Deng, J.; Cao, Y.; Li, D. Petrology and geochemistry of Silurian–Triassic sedimentary rocks in Tongling ore-cluster region of Eastern China: Their roles in the genesis of large stratabound skarn ore deposits. *Ore Geol. Rev.* **2015**, *67*, 255–263. [CrossRef]
35. Valley, J.W.; Lackey, J.S.; Cavosie, A.J.; Clechenko, C.C.; Spicuzza, M.J.; Basei, M.A.S.; Bindeman, I.N.; Ferreira, V.P.; Sial, A.N.; King, E.M.; et al. 4.4 billion years of crustal maturation: Oxygen isotope ratios of magmatic zircon. *Contrib. Mineral. Petrol.* **2005**, *150*, 561–580. [CrossRef]
36. Valley, J.W.; Kinny, P.D.; Schulze, D.J.; Spicuzza, M.J. Zircon megacrysts from kimberlite: Oxygen isotope variability among mantle melts. *Contrib. Mineral. Petrol.* **1998**, *133*, 1–11. [CrossRef]
37. Cavosie, A.J.; Kita, N.T.; Valley, J.W. Primitive oxygen-isotope ratio recorded in magmatic zircon from the Mid-Atlantic Ridge. *Am. Mineral.* **2009**, *94*, 926–934. [CrossRef]
38. Harlov, D.E. Apatite: A fingerprint for metasomatic processes. *Elements* **2015**, *11*, 171–176. [CrossRef]
39. Pan, L.C.; Hu, R.Z.; Wang, X.S.; Bi, X.W.; Zhu, J.J.; Li, C. Apatite trace element and halogen compositions as petrogenetic-metallogenic indicators: Examples from four granite plutons in the Sanjiang region, SW China. *Lithos* **2016**, *254*, 118–130. [CrossRef]
40. Pan, L.C.; Hu, R.Z.; Bi, X.W.; Wang, Y.; Yan, J. Evaluating magmatic fertility of Paleo-Tethyan granitoids in eastern Tibet using apatite chemical composition and Nd isotope. *Ore Geol. Rev.* **2020**, *127*, 103757. [CrossRef]
41. Qu, P.; Li, N.B.; Niu, H.C.; Yang, W.B.; Shan, Q.; Zhang, Z. Zircon and apatite as tools to monitor the evolution of fractionated I-type granites from the central Great Xing'an Range, NE China. *Lithos* **2019**, *348–349*, 105207. [CrossRef]
42. Qu, P.; Li, N.B.; Niu, H.C.; Shan, Q.; Weng, Q.; Zhao, X. Difference in the nature of ore-forming magma between the Mesozoic porphyry Cu-Mo and Mo deposits in NE China: Records from apatite and zircon geochemistry. *Ore Geol. Rev.* **2021**, *135*, 104218. [CrossRef]
43. Qu, P.; Yang, W.B.; Niu, H.C.; Li, N.B.; Wu, D. Apatite fingerprints on the magmatic-hydrothermal evolution of the Daheishan giant porphyry Mo deposit, NE China. *Geol. Soc. Am. Bull.* **2022**, *134*, 1863–1876. [CrossRef]
44. Guo, J.; Zhang, G.Y.; Xiang, L.; Zhang, R.Q.; Zhang, L.P.; Sun, W.D. Combined mica and apatite chemical compositions to trace magmatic-hydrothermal evolution of fertile granites in the Dachang Sn-polymetallic district, South China. *Ore Geol. Rev.* **2022**, *151*, 105168. [CrossRef]
45. Liu, Z.F.; Shao, Y.J.; Zhang, Y.; Wang, C. Geochemistry and geochronology of the Qingshanjiao granites: Implications for genesis of the Dongguashan Cu-(Au) ore deposit in the Tongling ore district, Eastern China. *Ore Geol. Rev.* **2018**, *99*, 42–57. [CrossRef]
46. Liu, Z.F.; Shao, Y.J.; Wang, C.; Liu, Q.Q. Genesis of the Dongguashan skarn Cu-(Au) deposit in Tongling, Eastern China: Evidence from fluid inclusions and H-O-S-Pb isotopes. *Ore Geol. Rev.* **2019**, *104*, 462–476. [CrossRef]
47. Zhang, J.D.; Liu, L.; Yu, Z.Q.; Yang, X.Y.; Liu, Z.F.; Li, H. Petrogenesis and metallogeny of the Dongguashan Cu-Au deposit in the Tongling ore-cluster region, the Lower Yangtze River Metallogenic Belt: Constraints from geochemistry and geochronology. *Geochemistry* **2021**, *81*, 125822. [CrossRef]
48. Zhou, T.F.; Fan, Y.; Feng, Y. Advances on petrogensis and metallogeny study of the mineralization belt of the middle and lower reaches of the Yangtze River Area. *Acta Petrol. Sin.* **2008**, *24*, 1665–1678, (In Chinese with English Abstract).
49. Zhai, Y.S.; Yao, S.Z.; Lin, X.D.; Zhou, X.N.; Wan, T.F.; Jin, F.Q.; Zhou, Z.G. *Fe–Cu (Au) Metallogeny of the Middle-Lower Changjiang Region*; Geological Publishing House: Beijing, China, 1992; p. 235.
50. Chen, C.J.; Chen, B.; Li, Z.; Wang, Z.Q. Important role of magma mixing in generating the Mesozoic monzodioritic-granodioritic intrusions related to Cu mineralization, Tongling, East China: Evidence from petrological and in situ Sr-Hf isotopic data. *Lithos* **2016**, *248–251*, 80–93. [CrossRef]
51. Chu, G.Z. Metallogenic System of Shizishan Cu-Au Ore-Field in Tongling Area and ITS prospecting significances. Ph.D. Thesis, China University of Geosciences, Beijing, China, 2003; pp. 1–100, (In Chinese with English Abstract).

52. Sláma, J.; Košler, J.; Condon, D.J.; Crowley, J.L.; Gerdes, A.; Hanchar, J.M.; Horstwood, M.S.A.; Morris, G.A.; Nasdala, L.; Norberg, N.; et al. Plešovice zircon—A new natural reference material for U-Pb and Hf isotopic microanalysis. *Chem. Geol.* **2008**, *249*, 1–35. [CrossRef]
53. Nasdala, L.; Hofmeister, W.; Norberg, N.; Mattinson, J.M.; Corfu, F.; Dörr, W.; Kamo, S.L.; Kennedy, A.K.; Kronz, A.; Reiners, P.W.; et al. Zircon M257—A homogeneous natural reference material for the ion microprobe U-Pb analysis of zircon. *Geostand. Geoanal. Res.* **2008**, *32*, 47–265. [CrossRef]
54. Li, X.H.; Liu, Y.; Li, Q.L.; Guo, C.H.; Chamberlain, K.R. Precise determination of Phanerozoic zircon Pb/Pb age by multicollector SIMS without external standardization. *Geochem. Geophys. Geosyst.* **2009**, *10*, Q04010.
55. Stacey, J.T.; Kramers, J.D. Approximation of terrestrial lead isotope evolution by a two-stage model. *Earth Planet. Sci. Lett.* **1975**, *26*, 207–221. [CrossRef]
56. Ludwig, K.R. *Users' Manual for Isoplot 3.70: A Geochronological Toolkit for Mircrosoft Excel*; Berkeley Geochronology Center Special Publication No. 4; Berkeley Geochronology Center: Berkeley, CA, USA, 2008.
57. Tang, G.Q.; Li, X.H.; Li, Q.L.; Liu, Y.; Ling, X.X.; Yin, Q.Z. Deciphering the physical mechanism of the topography effect for oxygen isotope measurements using a Cameca IMS-1280 SIMS. *J. Anal. At. Spectrom.* **2015**, *30*, 950–956. [CrossRef]
58. Li, X.H.; Long, W.G.; Li, Q.L. Penglai zircon megacrysts: A potential new working reference material for microbeam determination of Hf–O isotopes and U-Pb age. *Geostand. Geoanal. Res.* **2010**, *34*, 117–134. [CrossRef]
59. Liu, Y.S.; Hu, Z.C.; Gao, S.; Gunther, D.; Xu, J.; Gao, C.G.; Chen, H.H. In situ analysis of major and trace elements of anhydrous minerals by LA-ICP-MS without applying an internal standard. *Chem. Geol.* **2008**, *257*, 34–43. [CrossRef]
60. Li, X.H.; Liu, D.Y.; Sun, M.; Li, W.X.; Liang, X.R.; Liu, Y. Precise Sm–Nd and U-Pb isotopic dating of the super-giant Shizhuyuan polymetallic deposit and its host granite, Southeast China. *Geol. Mag.* **2004**, *141*, 225–231. [CrossRef]
61. Tanaka, T.; Togashi, S.; Kamioka, H.; Amakawa, H.; Kagami, H.; Hamamoto, T.; Yuhara, M.; Orihashi, Y.; Yoneda, S.; Shimizu, H.; et al. JNdi–1: A neodymium isotopic reference in consistency with LaJolla neodymium. *Chem. Geol.* **2000**, *168*, 279–281. [CrossRef]
62. Wang, Y.; Yang, X.Y.; Deng, J.H.; Liu, S.S.; Sun, C.; Hou, Q.; Wang, L.J. A comprehensive overview on the origin of intrusive rocks and polymetallic mineralization in the Tongling ore-cluster region, lower Yangtze River Metallogenic Belt: Geological and geochemical constraints. *Ore Geol. Rev.* **2021**, *141*, 104625. [CrossRef]
63. Middlemost, E.A.K. Naming materials in the magma/igneous rock system. *Earth Sci. Rev.* **1994**, *37*, 215–224. [CrossRef]
64. Sajona, F.G.; Maury, R.C.; Bellon, H.; Cotten, J.; Defant, M.J.; Pubellier, M. Initiation of subduction and the generation of slab melts in western and eastern Mindanao, Philippines. *Geology* **1993**, *21*, 1007–1010. [CrossRef]
65. Sun, S.S.; McDonough, W.F. Chemical and isotopic systematics of oceanic basalts: Implications for mantle composition and processes. *Geol. Soc.* **1989**, *42*, 313–345. [CrossRef]
66. Pearce, J.A.; Harris, N.B.; Tindle, A.G. Trace element discrimination diagrams for the tectonic interpretation of granitic rocks. *J. Petrol.* **1984**, *25*, 956–983. [CrossRef]
67. Hofmann, A.; Bolhar, R.; Dirks, P.; Jelsma, H. The geochemistry of Archaean shales derived from a Mafic volcanic sequence, Belingwe greenstone belt, Zimbabwe: Provenance, source area unroofing and submarine versus subaerial weathering. *Geochim. Cosmochim. Acta* **2003**, *67*, 421–440. [CrossRef]
68. Plank, T.; Langmuir, C.H. The chemical composition of subducting sediment and its consequences for the crust and mantle. *Chem. Geol.* **1998**, *145*, 325–394. [CrossRef]
69. Chen, J.F.; Yan, J.; Xie, Z.; Xu, X.; Xing, F.M. Nd and Sr isotopic compositions of igneous rocks from the Lower Yangtze Region in Eastern China: Constrains on sources. *Phys. Chem. Earth (A)* **2001**, *26*, 719–731. [CrossRef]
70. Yan, J.; Chen, J.F.; Xu, X.S. Geochemistry of Cretaceous mafic rocks from the Lower Yangtze region, eastern China: Characteristics and evolution of the lithospheric mantle. *J. Asian Earth Sci.* **2008**, *33*, 177–193. [CrossRef]
71. Ames, L.; Zhou, G.Z.; Xiong, B.C. Geochronology and isotopic character of ultrahigh-pressure metamorphism with implications for collision of the Sino-Korean and Yangtze cratons, central China. *Tectonics* **1996**, *15*, 472–489. [CrossRef]
72. Webster, J.D.; Piccoli, P.M. Magmatic apatite: A powerful, yet deceptive, mineral. *Elements* **2015**, *11*, 177–182. [CrossRef]
73. Pan, Y.; Fleet, M.E. Compositions of the apatite-group minerals: Substitution mechanisms and controlling factors. *Rev. Mineral. Geochem.* **2002**, *48*, 13–49. [CrossRef]
74. Piccoli, P.M.; Candela, P.A. Apatite in igneous systems. *Rev. Mineral. Geochem.* **2002**, *48*, 255–292. [CrossRef]
75. Wang, H.R.; Cai, K.D.; Sun, M.; Xia, X.P.; Lai, C.K.; Li, P.F.; Wan, B.; Zhang, Z.Y. Apatite as a magma redox indicator and its application in metallogenic research. *Lithos* **2022**, *422*, 106749. [CrossRef]
76. Pang, K.N.; Li, C.S.; Zhou, M.F.; Ripley, E.M. Abundant Fe–Ti oxide inclusions in olivine from the Panzhihua and Hongge layered intrusions, SW China: Evidence for early saturation of Fe–Ti oxides in ferrobasaltic magma. *Contrib. Mineral. Petrol.* **2008**, *156*, 307–321. [CrossRef]
77. Hoskin, P.W.O.; Kinny, P.D.; Wyborn, D.; Chappell, B.W. Identifying accessory mineral saturation during differentiation in granitoid magmas: An integrated approach. *J. Petrol.* **2000**, *41*, 1365–1396. [CrossRef]
78. Drummond, M.S.; Defant, M.J. A model for trondhjemite–tonalite–dacite genesis and crustal growth via slab melting: Archaean to modern comparisons. *J. Geophys. Res.* **1990**, *95*, 21503–21521. [CrossRef]
79. Martin, H. The adakitic magmas: Modern analogues of Archaean granitoids. *Lithos* **1999**, *46*, 411–429. [CrossRef]
80. Moyen, J.F. High Sr/Y and La/Yb ratios: The meaning of the "adakitic signature". *Lithos* **2009**, *112*, 556–574. [CrossRef]

81. Zhang, C.C.; Sun, W.D.; Wang, J.T.; Zhang, L.P.; Sun, S.J.; Wu, K. Oxygen fugacity and porphyry mineralization: A zircon perspective of Dexing porphyry Cu deposit, China. *Geochim. Cosmochim. Acta* **2017**, *206*, 343–363. [CrossRef]
82. Deng, J.H.; Yang, X.Y.; Qi, H.S.; Zhang, Z.F.; Mastoi, A.S.; Berador, A.E.G.; Sun, W.D. Early cretaceous adakite from the atlas porphyry Cu-Au deposit in Cebu Island, Central Philippines: Partial melting of subducted oceanic crust. *Ore Geol. Rev.* **2019**, *110*, 102937. [CrossRef]
83. Deng, J.H.; Yang, X.Y.; Zhang, L.P.; Duan, L.A.; Mastoi, A.S.; Liu, H. An overview on the origin of adakites/adakitic rocks and related porphyry Cu-Au mineralization, Northern Luzon, Philippines. *Ore Geol. Rev.* **2020**, *124*, 103610. [CrossRef]
84. Hernández-Uribe, D.; Hernández-Montenegro, J.D.; Cone, K.A.; Palin, R.M. Oceanic slab-top melting during subduction: Implications for trace-element recycling and adakite petrogenesis. *Geology* **2020**, *48*, 216–220. [CrossRef]
85. Petford, N.; Atherton, M. Na-rich partial melts from newly underplated basaltic crust: The Cordillera Blanca Batholith, Peru. *J. Petrol.* **1996**, *37*, 1491–1521. [CrossRef]
86. Guo, Z.F.; Wilson, M.; Liu, J.Q. Post-collisional adakites in south Tibet: Products of partial melting of subduction-modified lower crust. *Lithos* **2007**, *96*, 205–224. [CrossRef]
87. He, Y.S.; Li, S.G.; Hoefs, J.; Huang, F.; Liu, S.A.; Hou, Z.H. Post-collisional granitoids from the Dabie orogen: New evidence for partial melting of a thickened continental crust. *Geochim. Cosmochim. Acta* **2011**, *75*, 3815–3838. [CrossRef]
88. Li, N.B.; Niu, H.C.; Yang, W.B.; Lai, C.K.; Zhao, Z.H. Orogenic root delamination induced by eclogitization of thickened lower crust in the Chinese Western Tianshan: Constraints from adakites. *J. Geophys. Res. Solid Earth* **2019**, *124*, 11089–11104. [CrossRef]
89. Castillo, P.R.; Janney, P.E.; Solidum, R. Petrology and geochemistry of Camiguin Island, southern Philippines: Insights into the source of adakite and other lavas in a complex arc tectonic setting. *Contrib. Mineral. Petrol.* **1999**, *134*, 33–51. [CrossRef]
90. Richards, J.P.; Kerrich, R. Special paper: Adakite-like rocks: Their diverse origins and questionable role in metallogenesis. *Econ. Geol.* **2007**, *102*, 537–576. [CrossRef]
91. Ma, Q.; Zheng, J.P.; Xu, Y.G.; Griffin, W.L.; Zhang, R.S. Are continental "adakites" derived from thickened or foundered lower crust? *Earth Planet. Sci. Lett.* **2015**, *419*, 125–133. [CrossRef]
92. Bourdon, E.; Eissen, J.P.; Monzier, M.; Robin, C.; Martin, H. Adakite-like lavas from Antisana volcano (Ecuador): Evidence from slab melt metasomatism beneath the Andean Northern volcanic zone. *J. Petrol.* **2002**, *43*, 99–217. [CrossRef]
93. Wang, J.Z.; Li, J.W.; Zhao, X.F.; Qian, Z.Z.; Ma, C.Q. Genesis of the Chaoshan gold deposit and its host intrusion, Tongling area: Constraints from $^{40}Ar/^{39}Ar$ ages and elemental and Sr-Nd-O-C-S isotope geochemistry. *Acta Petrol. Sin.* **2008**, *24*, 1875–1888, (In Chinese with English Abstract).
94. Li, X.H.; Li, Z.X.; Li, W.X.; Wang, X.C.; Gao, Y. Revisiting the "C-type adakites" of the Lower Yangtze River Belt, central eastern China: In-situ zircon Hf–O isotope and geochemical constraints. *Chem. Geol.* **2013**, *345*, 1–15. [CrossRef]
95. Ge, X.Y.; Li, X.H.; Chen, Z.G. The geochemical characteristics and petrogenesis of Mesozoic high Sr-low Y type intermediate-acid igneous rocks in the east China: Constraint for the thickness of the east China. *Chin. Sci. Bull.* **2002**, *47*, 474–480, (In Chinese with English abstract).
96. Xiong, X.L.; Keppler, H.; Audétat, A.; Ni, H.; Sun, W.; Li, Y. Partitioning of Nb and Ta between rutile and felsic melt and the fractionation of Nb/Ta during partial melting of hydrous metabasalt. *Geochim. Cosmochim. Acta* **2011**, *75*, 1673–1692. [CrossRef]
97. Sun, W.D.; Hu, Y.H.; Kamenetsky, V.S.; Eggins, S.M.; Chen, M.; Arculus, R.J. Constancy of Nb/U in the mantle revisited. *Geochim. Cosmochim. Acta* **2008**, *72*, 3542–3549. [CrossRef]
98. Sun, W.D.; Ling, M.X.; Chung, S.L.; Ding, X.; Yang, X.Y.; Liang, H.Y.; Fan, W.M.; Goldfarb, R.; Yin, Q.Z. Geochemical constraints on adakites of different origins and copper mineralization. *J. Geol.* **2012**, *120*, 105–120. [CrossRef]
99. Rudnick, R.L.; Gao, S. Composition of the continental crust. *Treat. Geochem.* **2003**, *3*, 1–64.
100. Foley, S.F.; Barth, M.G.; Jenner, G.A. Rutile/melt partition coefficients for trace elements and an assessment of the influence of rutile on the trace element characteristics of subduction zone magmas. *Geochim. Cosmochim. Acta* **2000**, *64*, 933–938. [CrossRef]
101. Schmidt, M.; Dardon, A.; Chazot, G.; Vannucci, R. The dependence of Nb and Ta rutile–melt partitioning on melt composition and Nb/Ta fractionation during subduction processes. *Earth Planet. Sci. Lett.* **2004**, *226*, 415–432. [CrossRef]
102. Ding, X.; Lundstrom, C.; Huang, F.; Li, J.; Zhang, Z.M.; Sun, X.M.; Liang, J.L.; Sun, W.D. Natural and experimental constraints on formation of the continental crust based on niobium–tantalum fractionation. *Int. Geol. Rev.* **2009**, *51*, 473–501. [CrossRef]
103. John, T.; Klemd, R.; Klemme, S.; Pf¨ander, J.A.; Hoffmann, J.E.; Gao, J. Nb–Ta fractionation by partial melting at the titanite–rutile transition. *Contrib. Mineral. Petrol.* **2011**, *161*, 35–45. [CrossRef]
104. Bindeman, I.N.; Eiler, J.M.; Yogodzinski, G.M.; Tatsumi, Y.; Stern, C.R.; Grove, T.L.; Portnyagin, M.; Hoernle, K.; Danyushevsky, L.V. Oxygen isotope evidence for slab melting in modern and ancient subduction zones. *Earth Planet. Sci. Lett.* **2005**, *235*, 480–496. [CrossRef]
105. Xu, Z.W.; Lu, X.C.; Ling, H.F.; Lu, J.J.; Jiang, S.Y.; Nie, G.P.; Huang, S.S.; Hua, M. Study on metallogenic mechanism and time of hydrothermal superimposed transformation of Dongguashan stratified copper Deposit in Anhui Province. *Acta. Geol. Sin.* **2005**, *3*, 372, (In Chinese with English Abstract).
106. Lu, S.M. The Magmatism and Fluid Mineralization of Shizishan Copper-Gold Orefield of Tongling, Anhui Province. Ph.D. Thesis, Hefei University of Technology, Hefei, China, 2007; pp. 1–100, (In Chinese with English abstract).
107. Chen, K.; Shao, Y.J.; Zhang, J.K.; Zhang, Y.; Tan, H.J.; Zhang, Y.C.; Liu, Z.F. Garnet U-Pb geochronology and geochemistry reveal deposit types and fluid evolution: An example from the Dongguashan Cu-Au deposit, eastern China. *Ore Geol. Rev.* **2022**, *145*, 104883. [CrossRef]

108. Xiao, X.; Zhou, T.F.; White, N.C.; Zhang, L.J.; Fan, Y.; Chen, X.F. Multiple generations of titanites and their geochemical characteristics record the magmatic hydrothermal processes and timing of the Dongguashan porphyry-skarn Cu-Au system, Tongling district, Eastern China. *Miner. Depos.* **2021**, *56*, 363–380.
109. Xu, X.C.; Lu, S.M.; Xie, Q.Q.; Bai, L. SHRIMP Zircon U-Pb Dating for the Magmatic Rocks in Shizishan Ore-field of Tongling, Anhui Province, and Its Geological Implications. *Acta Geol. Sin.* **2008**, *82*, 500–510, (In Chinese with English Abstract).
110. Sun, W.D.; Bennett, V.C.; Eggins, S.M.; Arculus, R.J.; Perfit, M.R. Rhenium systematics in submarine MORB and back-arc basin glasses: Laser ablation ICP-MS results. *Chem. Geol.* **2003**, *196*, 259–281.
111. Thiéblemont, D.; Stein, G.; Lescuyer, J.L. Epithermal and porphyry deposits: The adakite connection. *C. R. L'acad. Sci. Paris* **1997**, *325*, 103–109.
112. Oyarzún, R.; Márquez, A.; Lillo, J.; López, I.; Rivera, S. Giant vs small porphyry copper deposits of Cenozoic age in northern Chile: Adakitic vs normal calc-alkaline magmatism. *Miner. Depos.* **2001**, *36*, 794–798. [CrossRef]
113. Ballard, J.R.; Palin, M.J.; Campbell, I.H. Relative oxidation states of magmas inferred from Ce(IV)/Ce(III) in zircon: Application to porphyry copper deposits of northern Chile. Contrib. *Mineral. Petrol.* **2002**, *144*, 347–364. [CrossRef]
114. Sun, W.D.; Huang, R.F.; Li, H.; Hu, Y.B.; Zhang, C.C.; Sun, S.J.; Zhang, L.P.; Ding, X.; Li, C.Y.; Zartman, R.E.; et al. Porphyry deposits and oxidized magmas. *Ore Geol. Rev.* **2015**, *65*, 97–131.
115. Sun, W.D.; Wang, J.T.; Zhang, L.P.; Zhang, C.C.; Li, H.; Ling, M.X.; Ding, X.; Li, C.Y.; Liang, H.Y. The formation of porphyry copper deposits. *Acta Geochim.* **2017**, *36*, 9–15.
116. Nadeau, O.; Willians-Jones, A.E.; Stix, J. Sulphide magma as a source of metals in arcrelated magmatic hydrothermal ore fluids. *Nat. Geosci.* **2010**, *3*, 501–505. [CrossRef]
117. Brounce, M.; Boyce, J.; McCubbin, F.M.; Humphreys, J.; Reppart, J.; Stolper, E.; Eiler, J. The oxidation state of sulfur in lunar apatite. *Am. Mineral.* **2019**, *104*, 307–312.
118. Chu, M.F.; Wang, K.L.; Griffin, W.L.; Chung, S.L.; O'Reilly, S.Y.; Pearson, N.J.; Iizuka, Y. Apatite composition: Tracing petrogenetic processes in Transhimalayan granitoids. *J. Petrol.* **2009**, *50*, 1829–1855.
119. Miles, A.J.; Graham, C.M.; Hawkesworth, C.J.; Gillespie, M.R.; Hinton, R.W.; Bromiley, G.D. Apatite: A new redox proxy for silicic magmas? *Geochim. Cosmochim. Acta* **2014**, *132*, 101–119.
120. Sha, L.K.; Chappell, B.W. Apatite chemical composition, determined by electron microprobe and laser-ablation inductively coupled plasma mass spectrometry, as a probe into granite petrogenesis. *Geochim. Cosmochim. Acta* **1999**, *63*, 3861–3881.
121. Konecke, B.A.; Fiege, A.; Simon, A.C.; Linsler, S.; Holtz, F. An experimental calibration of a sulfur-in-apatite oxybarometer for mafic systems. *Geochim. Cosmochim. Acta* **2019**, *265*, 242–258.
122. Sadove, G.; Konecke, B.A.; Fiege, A.; Simon, A.C. Structurally bound S^{2+}, S^{1+}, S^{4+}, S^{6+} in terrestrial apatite: The redox evolution of hydrothermal fluids at the Phillips mine, New York, USA. *Ore Geol. Rev.* **2019**, *107*, 1084–1096.
123. Ding, T.; Ma, D.S.; Lu, J.J.; Zhang, R.Q. Apatite in granitoids related to polymetallic mineral deposits in southeastern Hunan province, Shi-Hang zone, China: Implications for petrogenesis and metallogenesis. *Ore Geol. Rev.* **2015**, *69*, 104–117.
124. Qian, L.; Wang, Y.; Xie, J.C.; Sun, W.D. The Late Mesozoic granodiorite and polymetallic mineralization in southern Anhui Province, China: A perspective from apatite geochemistry. *Solid Earth Sci.* **2019**, *4*, 178–189.
125. Mathez, E.A.; Webster, J.D. Partitioning behavior of chlorine and fluorine in the system apatite-silicate melt-fluid. *Geochim. Cosmochim. Acta* **2005**, *69*, 1275–1286. [CrossRef]
126. McCubbin, F.M.; Kaaden, K.E.V.; Tart'ese, R.; Boyce, J.W.; Mikhail, S.; Whitson, E.S.; Bell, A.S.; Anand, M.; Franchi, I.A.; Wang, J. Experimental investigation of F, Cl, and OH partitioning between apatite and Fe-rich basaltic melt at 1.0–1.2 GPa and 950–1000 °C. *Am. Mineral.* **2015**, *100*, 1790–1802. [CrossRef]
127. Boyce, J.W.; Hervig, R.L. Apatite as a monitor of late-stage magmatic processes at Volcán Irazú, Costa Rica. *Contrib. Mineral. Petrol.* **2009**, *157*, 135–145.
128. Boyce, J.W.; Liu, Y.; Rossman, G.R.; Guan, Y.B.; Eiler, J.M.; Stolper, E.M.; Taylor, L.A. Lunar apatite with terrestrial volatile abundances. *Nature* **2010**, *466*, 466–470.
129. McCubbin, F.M.; Hauri, E.H.; Elardo, S.M.; Vander Kaaden, K.E.; Wang, J.; Shearer, C.K. Hydrous melting of the martian mantle produced both depleted and enriched shergottites. *Geology* **2012**, *40*, 683–686.
130. Tartése, R.; Anand, M.; Barnes, J.J.; Starkey, N.A.; Franchi, I.A.; Sano, Y. The abundance, distribution, and isotopic composition of hydrogen in the Moon as revealed by basaltic lunar samples: Implications for the volatile inventory of the Moon. *Geochim. Cosmochim. Acta* **2013**, *122*, 58–74.
131. Dingwell, D.B.; Hess, K.U.; Romano, C. Extremely fluid behavior of hydrous peralkaline rhyolites. *Earth Planet. Sci. Lett.* **1998**, *158*, 31–38.
132. Filiberto, J.; Treiman, A.H. The effect of chlorine on the liquidus of basalt: First results and implications for basalt genesis on Mars and Earth. *Chem. Geol.* **2009**, *263*, 60–68.
133. Bai, T.B.; Koster Van Groos, A.F. The distribution of Na, K, Rb, Sr, Al, Ge, Cu, W, Mo, La, and Ce between granitic melts and coexisting aqueous fluids. *Geochim. Cosmochim. Acta* **1999**, *63*, 1117–1131.
134. Hezarkhani, A.; Williams-Jones, A.E.; Gammons, C.H. Factors controlling copper solubility and chalcopyrite deposition in the Sungun porphyry copper deposit, Iran. *Miner. Depos.* **1999**, *34*, 770–783. [CrossRef]
135. Archibald, S.M.; Migdisov, A.A.; Williams-Jones, A.E. The stability of Au-chloride complexes in water vapor at elevated temperatures and pressures. *Geochim. Cosmochim. Acta* **2001**, *65*, 4413–4423. [CrossRef]

136. Lassiter, J.C.; Hauri, E.H.; Nikogosian, I.K.; Barsczus, H.G. Chlorine–potassium variations in melt inclusions from Raivavae and Rapa, Austral Islands: Constraints on chlorine recycling in the mantle and evidence for brine-induced melting of oceanic crust. *Earth Planet. Sci. Lett.* **2002**, *202*, 525–540.
137. Blevin, P.L.; Chappell, B.W. The role of magma sources, oxidation states and fractionation in determining the granite metallogeny of eastern Australia. *Earth Environ. Sci. Trans. R. Soc. Edinb.* **1992**, *83*, 305–316.
138. Stroncik, N.A.; Haase, K.M. Chlorine in oceanic intraplate basalts: Constraints on mantle sources and recycling processes. *Geology* **2004**, *32*, 945–948.